THE JOURNAL OF PHYSICAL CHEMISTRY C

Article

pubs.acs.org/JPCC

In situ X-ray Scattering and Dynamical Modeling of Pd Catalyst Nanoparticles Formed in Flames

Juan Wang,[†,‡,$] Sönke Seifert,[§] Randall E. Winans,[*,§] Erik Tolmachoff,[∥] Yuxuan Xin,[⊥] Dongping Chen,[#] Hai Wang,[#] and Scott L. Anderson[‡]

[†]The Peac Institute of Multiscale Sciences, Chengdu, Sichuan 610207, China

[‡]Department of Chemistry, University of Utah, Salt Lake City, Utah 84112, United States

[§]X-ray Science Division, Advanced Photon Source, Argonne National Laboratory, Argonne, Illinois 60439, United States

[∥]Aerospace and Mechanical Engineering, University of Southern California, Los Angeles, California 90089, United States

[⊥]Mechanical and Aerospace Engineering, Princeton University, Princeton, New Jersey 08544, United States

[#]Mechanical Engineering, Stanford University, Stanford, California 94305, United States

[$]Key Laboratory of Advanced Technologies of Materials, Ministry of Education, Southwest Jiaotong University, Chengdu, Sichuan 610031, China

ABSTRACT: It has previously been demonstrated that organopalladium precursors can break down under combustion conditions, forming nanoparticles that catalyze ignition. Here, we use in situ small-angle X-ray scattering (SAXS) to probe the formation and growth of palladium nanoparticles in an ethylene flame doped with 28 ppm (mol) of Pd(acetate)$_2$. The particles appear to nucleate in the flame front and are observed by SAXS to grow in size and mass in the high-temperature region of the flame (~2200 K) with median diameters that evolve from 1.5 to 3.0 nm. Transmission electron microscopy of particles collected on a grid located outside the flame shows that the particles are metallic palladium with sizes comparable to those determined by SAXS. Molecular dynamics simulation of particles of selected sizes indicates that at the flame temperature the particles are molten and the average mass density of the particle material is notably smaller than that of bulk, liquid Pd at the melting point. Both experimental and computational results point to homogeneous nucleation and particle−particle coalescence as mechanisms for particle formation and growth. Aerosol dynamics simulation reproduces the time evolution of the particle size distribution and suggests that a substantial fraction of the particles must be electrically charged during their growth process.

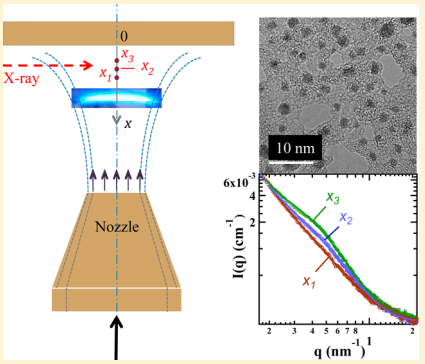

1. INTRODUCTION

Rapid ignition and combustion are required for propulsion applications such as hypersonic or pulse-detonation engines, and catalysis is an obvious approach to improving kinetics. For such applications, the flow rates are too high to allow use of fixed catalyst beds or structures, and the catalysts would also tend to deactivate rapidly under engine conditions. Another approach that has received considerable recent interest is use of catalysts or catalyst precursors dissolved in the fuel.[1−10] This approach potentially results in high specific surface area catalyst nanoparticles that are intimately dispersed in the fuel, such that the kinetics are not impeded by mass and heat transport limitations. In an ideal system, the fuel-soluble catalyst might catalyze endothermic reaction in the fuel system, needed for engine cooling, and then go on to catalyze ignition and combustion after the catalyst-loaded fuel enters the combustor.

Two approaches to delivering nanoparticle catalysts with the fuel have been reported. One uses organic ligands functionalized on catalyst nanoparticles to achieve solubility,[5−9] and the other employs a fuel-soluble organometallic precursor that can transform itself rapidly to catalyst nanoparticles in a reacting flow.[2−4,10] In particular, both nanoparticles and organometallic compounds containing Pd have been proposed for this application.[2−4,6,9,10] For example, Shimizu et al.[3] and Van Devener et al.[4] demonstrated that an organopalladium compound injected into a gas-phase flow reactor with fuel was effective at catalyzing methane ignition and that ignition required formation of metallic Pd nanoparticles with a monolayer of oxide on the surface.

To further develop this approach, it is critical to understand the fundamental behavior of particle nucleation and growth in flames, both in terms of the mechanism of particle formation and the chemical nature of the resulting particles. Clearly, if such particles are to catalyze ignition, then either the particles must begin to form in the fuel, prior to injection, or the kinetics for particle formation in flames must be fast. Previously, we reported a synchrotron small-angle X-ray scattering (SAXS) study of in situ formation and growth of Pd nanoparticles from

Received: February 5, 2015
Revised: July 21, 2015
Published: July 21, 2015

DOI: 10.1021/acs.jpcc.5b01226
J. Phys. Chem. C 2015, 119, 19073−19082

fuel-soluble precursor in hot liquid fuel.[10] Here, we use SAXS to study the second part of the problem—particle nucleation and growth in flames doped with a Pd organometallic precursor.

The high flux and collimation provided by synchrotron radiation has made SAXS an effective method even for small sample volumes and dilute and low contrast samples. This technique was successfully used for studying soot particles[11−19] and silica nanoparticles[20,21] in flames. It is reported that particles in flame can be detected at volume fractions as low as 10^{-6},[15,16,20,21] and particle sizes ranging from 1 nm to a few hundred nanometers can be followed using this technique. In this paper, we will present the first detection of particles in flame with total volume fraction that can be $<10^{-8}$ using in situ SAXS and report particle size distributions obtained by fitting SAXS profiles. For these purposes, a premixed stagnation flow ethylene flame doped with $Pd(acetate)_2$ is employed to generate Pd nanoparticles in the flame. To assist data interpretation, flame simulation was used to understand the gas-phase composition and temperature−time history for particle formation and growth. Molecular dynamics is utilized to understand the thermal expansion of the particles in the high-temperature flame and to provide particle properties necessary for SAXS data interpretation. The Smoluchowski coalescence equation is solved to understand the mechanism underlying particle size evolution.

2. EXPERIMENTAL AND COMPUTATIONAL METHODOLOGY

2.1. Theory of SAXS. For a dilute system without particle interactions, the scattered intensity I depends on the number density N, shape, and size of the particles.[22,23]

$$I(q) = N(\Delta\rho)^2 F(q) \tag{1}$$

The scattering vector q is defined as

$$q = (4\pi/\lambda)\sin\Theta \tag{2}$$

where λ is the wavelength of the incident X-rays and Θ is the half angle of the scattering. In eq 1, ρ is the scattering length density, defined as

$$\rho = r_e \rho_e \tag{3}$$

where r_e is the classical electron radius and also the Thomson scattering length (2.818×10^{-13} cm) and ρ_e is the electron density which is described as

$$\rho_e = n_e \rho_m / m_1 \tag{4}$$

In eq 4, n_e is the number of electrons in the constituent atom or molecule, ρ_m is the mass density of the particle material, and m_1 is the mass of the monomer or constituent molecule/atom of the particle. $\Delta\rho$ is the difference of the scattering length density between particles and a medium where particles are embedded. For crystalline palladium at room temperature, the scattering length density ρ is 8.814×10^{11} cm^{-2}, which is substantially larger than that of air at room temperature and atmospheric pressure ($\sim 10^8$ cm^{-2}). Hence, it was assumed that $\Delta\rho \cong \rho$. In principle, the mass density of the particle material varies with temperature and the size of the particles in the few nanometer size range. Here, we obtain the ρ_m value from molecular dynamics simulation, as will be discussed below.

$F(q)$ is the form factor, which is a function of the shape, size, and polydispersity of the particles. For spherical particles, the form factor can be expressed as eq 5[22−24]

$$F(q, r) = \left(\frac{4}{3}\pi r^3\right)^2 \{3[\sin(qr) - qr\cos(qr)]/(qr)^3\}^2 \tag{5}$$

where r is the particle radius. The form factor functions for other particle shapes can be found in the literature.[22−24]

In the case of polydisperse particles, the mean form factor can be rewritten as an integral over the size distribution[22,24]

$$\bar{F}(q, \bar{r}) = \int_0^\infty F(q, r)P(r)\,dr \tag{6}$$

where $P(r)$ is the probability of having scatterers with size r, and $\bar{r}$ is the mean particle size. The probability distribution satisfies the normalization condition that $\int_0^\infty P(r)dr \equiv 1$. Here, $P(r)$ was assumed to be log-normal as this is expected for particles formed in a gas-phase nucleation and growth mechanism that is dominated by particle−particle coalescence[25,26]

$$P(r) = \frac{N}{\sqrt{2\pi}\, r \ln\sigma_g} \exp\left[-\frac{(\ln r - \ln\langle r\rangle)^2}{2(\ln\sigma_g)^2}\right] \tag{7}$$

where N is the number density and σ_g is the geometric standard deviation of $P(r)$.

When particles form large aggregates whose size is outside the detection limit, only the tail of the form factor scattering will be observed in the measurement. This typically gives power law scattering, $I(q) \propto q^{-D_f}$, where the exponent D_f is related to the surface morphology of the clusters.[23]

If the sample system includes small particles and also aggregates larger than the detection limit, then including all contributions above, the scattered intensity curve should show power law scattering at low q, with a superimposed "knee" feature at high q from the small particles. In this case, the scattered intensity should be written as

$$I(q) = N(\Delta\rho)^2[cq^{-D_f} + \bar{F}(q, \bar{r})] \tag{8}$$

2.2. Experimental Section. A premixed, flat flame was stabilized by issuing a gaseous combustible mixture through an aerodynamic nozzle with a 1 cm exit diameter in a stagnation flow field, as shown in Figure 1. Details of the setup can be found elsewhere.[27,28] The combustion mixture was formed from the following gases at the indicated flow rates, C_2H_4 (0.257 L/min), O_2 (1.34 L/min), and N_2 (3.80 L/min), with the palladium precursor added as discussed below (Table 1). A shroud flow of N_2 at 3.89 L/min, passing through a concentric tube, kept the flame isolated from the surrounding air. The flow impinged on a water-cooled plate positioned 3.36 cm above the burner nozzle. The plate acted as a flow-stagnation surface to stabilize the flame, and its temperature during operation was ~150 °C, as measured using a K-type thermocouple. In the absence of the Pd precursor, the visible flame was about 0.2 cm thick, beginning ~2.5 cm away from the burner surface, and extending to within ~0.86 cm of the stagnation surface (Table 1).

$Pd(acetate)_2$ was used as the precursor, dissolved in acetone, and pumped into an aerosol generator (SONAER, Inc., 241PG), which produced droplets with diameter around 3 μm. The droplets were entrained in a flow of 121 mL/min of N_2 passing through the aerosol generator and then mixed with

DOI: 10.1021/acs.jpcc.5b01226
J. Phys. Chem. C 2015, 119, 19073−19082

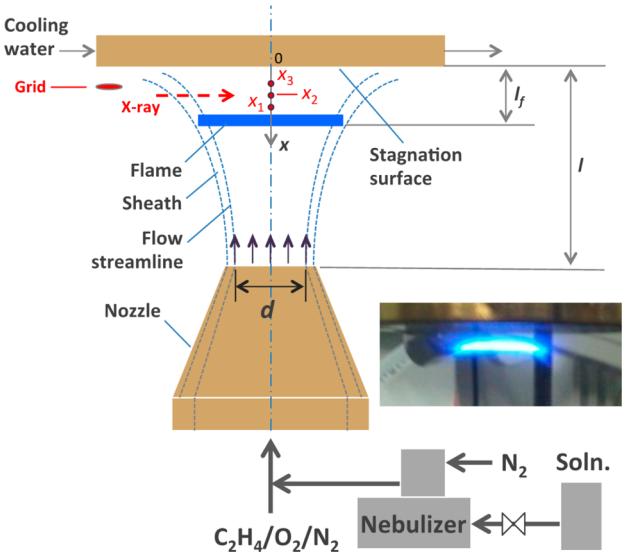

Figure 1. Schematic of the experimental setup. SAXS signals are acquired at three positions between the flame and the stagnation surface (x_1 = 0.76 cm, x_2 = 0.56 cm, and x_3 = 0.36 cm).

Table 1. Flame Conditions

mole fractions				
C_2H_4	O_2	N_2	CH_3COCH_3	$Pd(acetate)_2$
0.046	0.239	0.698	0.017	2.8×10^{-5}

equivalence ratio, φ	0.86
cold gas velocity at nozzle exit	117 cm/s (STP)
annular N_2 sheath flow rate	3.89 L/min (STP)
temperature at nozzle exit, T_0	298 K
stagnation surface temperature, T_s	~423 K
adiabatic flame temperature	2415 K (computed)
maximum flame temperature, T_f	2380 K (computed)
pressure, p	1 atm
nozzle diameter, d	1 cm
nozzle-to-stagnation surface distance, l	3.36 cm

the main combustion gas flow before entering the burner. The aerosolization rate of the solution was 0.29 mL/min measured based by the consumption rate of the solution in the aerosol generator.

The in situ SAXS measurements were carried out at beamline 12-ID-C at the Advanced Photon Source (APS) at Argonne National Laboratory. The incident X-ray energy was 12 keV, and the beam size was 0.06 cm in width and 0.01 cm in height. The corresponding X-ray wavelength is 0.1033 nm. The sample-to-detector distance was approximately 2 m. A home-built 1024 × 1024 pixel 2D platinum CCD detector was used to record the SAXS images from the sample.

As a control, measurements were made on flames with the same reactant flow, but without the $Pd(acetate)_2$ aerosol addition. The SAXS background includes scattering from air and instrument windows. The experiments were challenging because the concentration of particles in the flame is rather low. Therefore, reducing background from air scattering is critical; however, if the windows are too close to the flame, particles deposit on them, causing growing background during the measurements. In the final configuration, the distance between the two windows was 8.5 cm, with the flame centered between them.

Samples of particles were also collected for transmission electron microscopy (TEM) by positioning a grid close to the edge of the stagnation plate, about 2.5 cm away from the flame edge (Figure 1). TEM measurements were done at the Center of Nanoscale Materials (CNM) at Argonne National Laboratory.

2.3. Flame and Aerosol Dynamics Modeling. One-dimensional flame modeling along the center line of the stagnation flame was performed using the program OPPDIF[29] through the CHEMKIN suite of computer codes. OPPDIF calculates the temperature, species mole fractions, and axial and radial velocity components. The gas-phase reaction chemistry and transport model employs USC Mech II.[30] The simulation used a multicomponent transport formula including thermal diffusion.

Nucleation and growth of palladium particles are simulated by direct solution of the Smoluchowski equations, using the temperature−space−time history computed with OPPDIF. For particles formed from homogeneous nucleation, the kinetic process may be described by

$$\frac{dn_1}{dt} = -n_1 \sum_{j=1}^{\infty} \varepsilon \beta_{1,j} n_j \tag{9}$$

and

$$\frac{dn_i}{dt} = \frac{1}{2} \sum_{j=1}^{i-1} \varepsilon \beta_{j,i-j} n_j n_{i-j} - n_i \sum_{j=1}^{\infty} \varepsilon \beta_{i,j} n_j \quad (i = 2, 3, ..., \infty) \tag{10}$$

where n_i is the number density of particles containing i number of Pd atoms, t is the time, $\beta_{i,j}$ is the coalescence coefficient between particles i and j,

$$\beta_{i,j} = \sqrt{\frac{8\pi k_B T}{m_1}} \left(\frac{4m_1}{3\pi\rho_m} \right)^{2/3} (i^{-1} + j^{-1})^{1/2} (i^{1/3} + j^{1/3})^2 \tag{11}$$

ε is the collision enhancement factor due to particle−particle interactions, and k_B is the Boltzmann constant. Here, we neglect the size dependence of ε because the variation of the size of interest in the current work is small. The simulation assumed unit sticking probability. Equations 9 and 10 are solved by direct numerical integration of roughly 20000 differential equations.[31]

2.4. Molecular Dynamics. MD simulations were carried out to understand the effects of the shape and phase state of the particles and the mass density of the particle material on the SAXS data interpretation. The interactions among atoms are described by a tight-binding potential function for Pd with a plain 1 nm cutoff.[32] The initial positions of a prescribed number of atoms are constructed from an fcc lattice of the bulk Pd, truncating atoms that lie outside of a sphere of radius r. All simulations were performed using an in-house code developed previously.[33] The equations of motion were integrated using Beeman's leapfrog algorithm[34] with the time step equal to 1 fs. We first used a NVT ensemble to equilibrate the particle for 10 ps in vacuo, and the kinetic energy was rescaled to the target temperature every 0.5 ps. The simulations were further extended in a NVE ensemble for 90 ps, and the trajectories were analyzed to estimate the density of Pd nanoparticles. We simulated Pd nanoparticles with 35, 123, and 273 atoms. Each particle was simulated three times with the initial velocities of

DOI: 10.1021/acs.jpcc.5b01226
J. Phys. Chem. C 2015, 119, 19073−19082

the atoms distributed according to the Boltzmann distribution at 2000 K. The results do not show obvious differences for the mass density. The rotational motions of the particles are deactivated in most of the simulations, since the mass density was found to be insensitive to rotation.

To calculate the particle density, the volumes of Pd nanoparticles were estimated using a Monte Carlo (MC) integration routine.[35] For this calculation, the radius of a Pd atom is assumed to be equal to 0.254 nm, i.e., the sum of van der Waal radius of a Pd crystal (0.202 nm)[36] and half of the X-ray wavelength of the corresponding SAXS experiments (0.52 nm). A second, rolling-ball scheme[37] was also used to verify the MC approach, and the results show no obvious difference.

3. RESULTS AND DISCUSSION

3.1. Scattering Signals and Composition. The X-ray beam was passed horizontally (i.e., radially) through the flame, parallel to the stagnation surface, and scattered X-ray intensities were obtained for several beam positions relative to the stagnation surface (dimension "x" in Figure 1). Accordingly, increasing x corresponds to decreasing residence time. Water was used as a standard to calibrate the measured intensities to obtain absolute intensities for particles per unit volume. Figure 2 shows the absolute intensity profiles corresponding to the

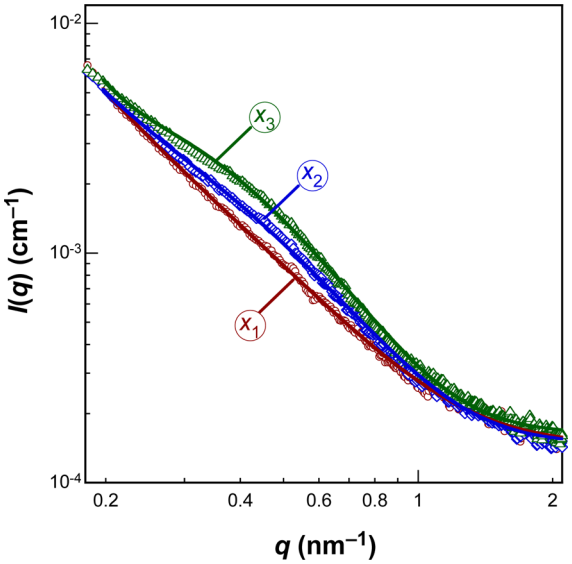

Figure 2. Experimental (symbols) and modeled (lines) scattered intensities at the three distances from the stagnation surface (see Figure 1).

positions: $x_1 = 0.76$, $x_2 = 0.56$, and $x_3 = 0.36$ cm, taken using 5 s exposure time. The points are the experimental data, and the lines through the points are fits used to extract information about the particle size distribution (see below). The low q power law scattering is from particles whose size is over several hundred nanometers and is out of our measurement range. The scattering becomes flat at high q because either the particles are too small or the particle concentration is too low to be detected. At positions further away from the stagnation surface, e.g., $x > 0.8$ cm, the scattered intensity curves only show power law scattering at low q and flat scattering at high q. However, the scattering from nanoparticles clearly can be observed as "knee" features at q around 0.45 nm^{-1}, with intensity growing from x_1 to x_3, i.e., as the residence time in the flame increases.

The mass density of the particle material, and the composition and shape information are needed in order to extract quantitative particle size information from the SAXS profiles. Decomposition of the Pd(acetate)$_2$ precursor may lead to formation of particles of metallic Pd and/or of PdO.[38] TEM measurements were made for particles collected on TEM grids located 2.5 cm away from the edge of the flame. The low-magnification and high-resolution TEM images of the particles are presented in Figure 3. The TEM image in Figure 3a shows

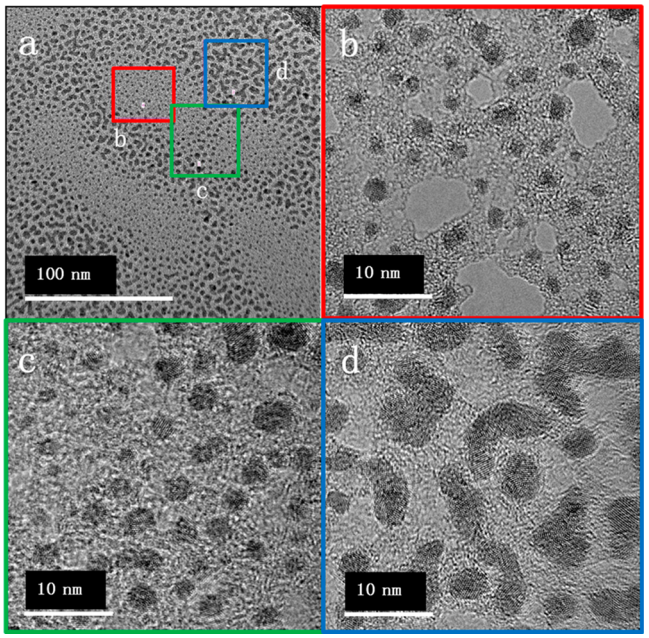

Figure 3. Low-magnification (a) and high-resolution (b–d) TEM images of particles collected about 2.5 cm away from the edge of the flame.

there are particles with different size ranges and features. The primary particles are roughly spherical. We carried out HRTEM for three small areas (b–d). The small primary particles in areas b and c range in size from 2 to 5 nm (Figure 3b,c). Area d shows somewhat larger, irregularly shaped particles that appear to be aggregated from two or more primary particles, and these aggregates show features that are indicative of mobility of the surface atoms, leading to neck filling and particle–particle coalescence. Since the particles in the flame are mostly molten and their coagulation would coalesce the particles, the aggregates observed were probably made at the time the particles were deposited and collected on the grid. For each area in Figure 3a, we obtained selected-area electron diffraction patterns (SAED), all of which were identical within the signal-to-noise level (Figure 4). The four diffraction rings were assigned to the (111), (200), (220), and (311) diffraction of fcc of Pd,[39] which confirms that at least the cores of the particles are crystalline, metallic Pd, presumably formed by crystallization of the molten particles as they are cooled before reaching the TEM grid. No PdO or other Pd compounds are observed in this measurement. Clearly, even though these particles were collected outside the flame, where the temperature is lower than 500 °C and oxygen is abundant, the bulk of the particles remain as metallic Pd. This observation suggests that the particles in the flame are also Pd and that kinetics for Pd oxidation are too slow to convert them to PdO before they were collected and examined by TEM. Note that the SAED

DOI: 10.1021/acs.jpcc.5b01226
J. Phys. Chem. C 2015, 119, 19073–19082

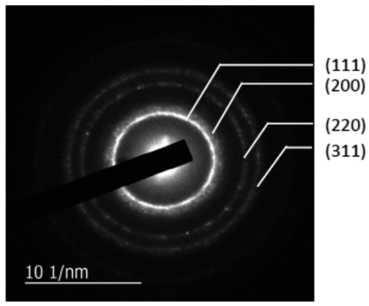

Figure 4. SAED pattern for particles from the flame, indicating that the particles are crystalline, metallic Pd.

measurements do not preclude the surface of the particles having a thin oxide layer, and indeed, we previously used XPS to show that metallic Pd particles formed in a flow reactor did have a roughly monolayer of surface oxide under high temperature conditions.[4]

3.2. Flame Structure. Various flame properties, including the measured gas temperatures at the nozzle exit and stagnation surface, are shown in Table 1. The adiabatic and maximum flame temperatures are computed results. The calculated convective velocity v_c and temperature T for the base flame are shown in Figure 5 as a function of distance from the

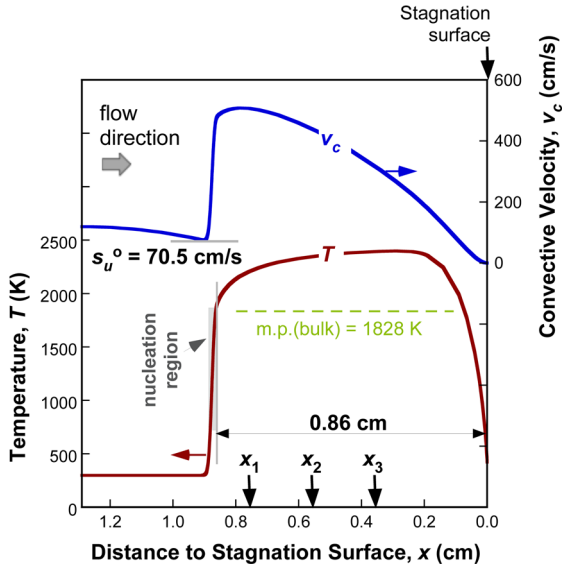

Figure 5. Convective velocity and temperature calculated for the base flame with a stagnation temperature of 423 K. Also shown is the laminar flame speed of the unburned mixture and the melting point of bulk Pd.[41]

stagnation surface. As indicated, the laminar flame speed computed for the unburned mixture (s_u° = 70.5 cm/s) is about 6% lower than the minimum axial velocity, as expected due to positive flow stretch.[40] In the flame front the temperature rises sharply: from 300 to 2000 K in 0.04 cm. The particles are expected to nucleate in that region ($x \sim 0.9$ cm), and they grow mostly in a wider spatial region of nearly constant temperature, around 2200 to 2300 K for $x \sim 0.8$ to 0.1 cm. The three positions of SAXS measurements (x_1, x_2, and x_3) fall in that nearly constant temperature region, where the gas temperature is higher than the melting point of bulk Pd (mp = 1828 K).[41] Because nanoparticles are expected to have melting points even lower than that of the bulk-phase material,[42] the Pd particles detected in situ by SAXS should be in the molten state. Solidification does not occur until at least $x \sim 0.05$ cm from the stagnation surface. Most of the particles are expected to undergo surface deposition due to the sharp temperature gradient, resulting in a strong thermophoretic force acting on the particles in the region where temperature drops sharply. As shown in Figure 6, chemically the region where particle size

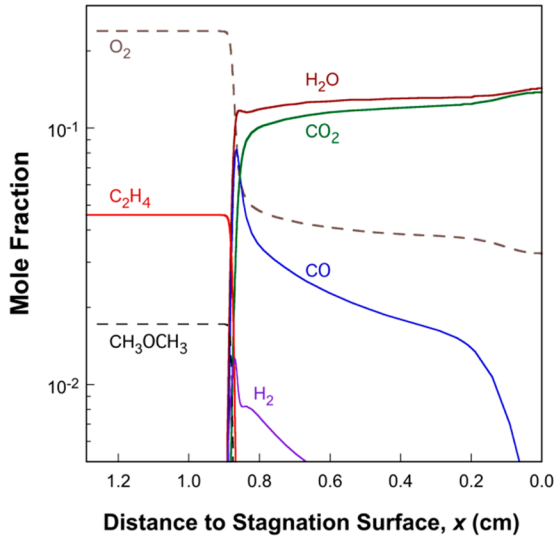

Figure 6. Major species profiles computed for the base flame.

growth is expected to occur is dominated by CO_2 and H_2O, and excess O_2 which is not entirely consumed because the experiments were conducted in fuel lean conditions. Some CO is present but its concentration is too small to have any impact on the growth process. From the perspective of modeling particle nucleation and growth, this is a nearly constant-temperature reactor in the spatial region of interest.

3.3. Mechanism. Two limiting mechanisms are possible for production of the Pd particles observed in the flame. The first involves drying of the $Pd(acetate)_2$-containing aerosol droplets, followed by condensed-phase decomposition of the $Pd(acetate)_2$ to generate a Pd particle. If we assume that the aerosol droplets remain intact as they dry, then from 3 μm droplets of the 0.61 Wt% $Pd(acetate)_2$ acetone solution we would expect Pd particles of about 170 nm diameter. This is much larger than the experimentally observed size. Of course, droplet fragmentation followed by subsequent drying is also possible, but the resulting particle size distribution is expected to be significantly larger than the observed size distribution, an issue to be discussed in more details later. The other limiting mechanism involves aerosol evaporation followed by gas-phase decomposition of $Pd(acetate)_2$ to produce Pd vapor that nucleates into Pd clusters, which subsequently grow by some combination of Pd vapor deposition and particle−particle coalescence.

Thermal decomposition of solid-phase $Pd(acetate)_2$ in N_2 or O_2 starts at 500 K, with an apparent activation energy of 27.4 kcal/mol.[39] Based on this activation energy value, the time scale of $Pd(acetate)_2$ dissociation is roughly 0.01 ms at 750 K assuming the frequency factor to be 10^{13} s^{-1}. The dissociation can lead to Pd and/or PdO. The bond dissociation energy of PdO(v) is 56 ± 3 kcal/mol, thus it becomes unstable at high temperatures.[43] Assuming that the frequency factor of PdO

DOI: 10.1021/acs.jpcc.5b01226
J. Phys. Chem. C 2015, 119, 19073−19082

dissociation is also 10^{13} s^{-1}, we estimate the dissociation rate constant to be 7×10^4 and 2×10^6 s^{-1} at 1500 and 1800 K, respectively. Thus, even if PdO(v) is produced from the thermal decomposition of $Pd(acetate)_2$, it would dissociate to form elemental Pd above 1500 K in roughly 0.01 ms.

The rate constant for the reaction between the ground-state Pd(v) with O_2

$$Pd(a^1S_0) + O_2 \rightarrow PdO_2(^3A'')$$

has also been reported.[44] Theoretical analysis of the measured rate constant shows that the bond energy of PdO_2(v) is 23 kcal/mol and, thus, is too small to avoid dissociation above 700 K. In other words, vapor-phase Pd remains as elemental Pd at flame temperatures, even in the presence of O_2.

A detailed reaction mechanism emerges from the above discussion. In the nucleation region that spans from roughly 750 to 1800 K (marked by the narrow, shaded area of Figure 5), $Pd(acetate)_2$ undergoes thermal decomposition

$$Pd(acetate)_2 \rightarrow Pd + 2CH_3C(O)O$$
$$\rightarrow PdO + CH_3C(O)O + CH_3CO$$

PdO dissociates into elemental Pd above around 1500 K. Condensation reactions of Pd(v) produce clusters:

$$Pd + Pd \rightarrow Pd_2$$

$$Pd + Pd_2 \rightarrow Pd_3$$

and the clusters may coalesce to form larger clusters or particles:

$$Pd_x + Pd_y \rightarrow Pd_{x+y}$$

Of course, PdO(v) also may be involved in the nucleation processes at least during the early stage of particle formation, resulting in clusters that are partially oxygenated. If formed, these particles would be reduced to pure Pd particles quickly because of a large equilibrium constant, K_p is 2.2×10^{-3} atm, at 909 K and 0.64 atm at 1124 K[45] for the reaction

$$2PdO(s) \rightarrow 2Pd(s) + O_2$$

In air, the preferred thermodynamic state is PdO below 900 K, but metallic Pd is favored above 1100 K.[3]

The above mechanism also is consistent with the TEM observation of particle sizes. To illustrate this point, we show in Figure 7 the particle residence time evaluated from the total velocity (v), which is the sum of the flow convective velocity (v_c) and particle thermophoretic velocity (v_t) along the flame centerline. The thermophoretic velocity was calculated using the formula of Li and Wang.[46] Assuming that $Pd(acetate)_2$ decomposition and Pd nucleation begins to occur when the gas temperature reaches 750 K, the time available for particle production is estimated to be t_1 = 0.27 ms, t_2 = 0.69 ms, and t_3 = 1.25 ms for the three sampling positions, i.e., x_1, x_2, and x_3, respectively. These times are uncertain by at most ~0.1 ms, which is the flow time through the flame front, where the temperature increases from 700 to 2000 K (i.e., the shaded area of Figure 5). Assuming that the size evolution follows roughly temperature-independent coalescence kinetics, the particle number density is estimated to be N_t = 22, 8 and 4×10^{11} cm^{-3} for x_1, x_2, and x_3, respectively. In this estimate, we use the following equation

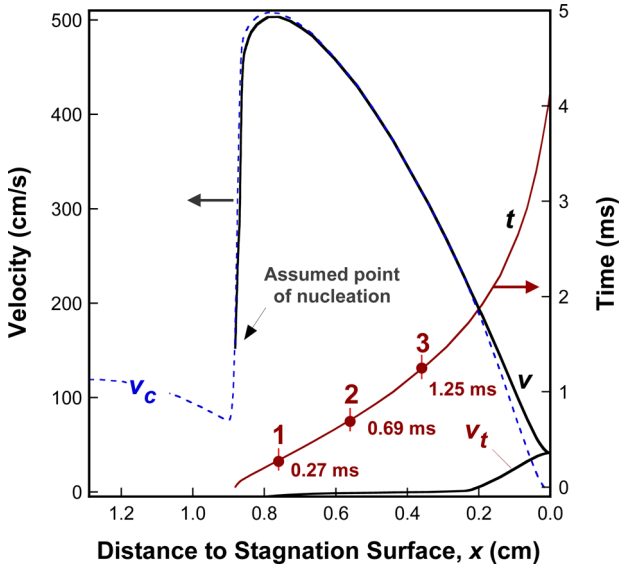

Figure 7. Convective (v_c), thermophoretic (v_t), and total (v) velocities along the flame centerline and the particle residence time in flames. Also shown are the three X-ray measurement positions (1, 2, and 3) and their respective time from the onset of particle nucleation.

$$N_t = \frac{N_0}{1 + 2\beta N_0 t} \quad (12)$$

where β (~10^{-9} cm^3/s) is the coalescence kernel and N_0 (~3×10^{14} cm^{-3}) is the initial precursor concentration. Using a mass density value for bulk Pd at its melting point (ρ_m = 10.38 g/cm^{-3}), we converted the number density values to the corresponding average particle diameters, which are 1.6, 2.3, and 2.8 nm, respectively. These values are consistent with the TEM observations (Figure 3) which show primary particle sizes in the few nanometer range. Detailed aerosol dynamics simulations are discussed below.

3.4. Particle Shape and Mass Density. Figure 8 presents snapshots of a 273-atom Pd nanoparticle at 2000 K as

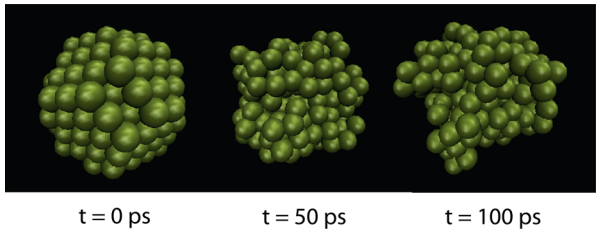

Figure 8. MD snapshots of a 273-atom Pd nanoparticle at 2000 K.

computed by MD. This is a particle that would be 2 nm in diameter if the mass density (10.38 g/cm^3) is equal to that at the melting point of bulk palladium. Initially, the particle shape was a rough sphere, but because of the kinetic energy of Pd atoms it quickly becomes somewhat irregular. The particles under this temperature are clearly molten and as such the instantaneous size varies as a function of time to an extent. Figure 9 shows the distribution of particle volume for the three particle sizes tested. Clearly the mean particle volume is larger than what would be calculated from the mass density of bulk liquid Pd. For example, the 273-atm particle has an average mass density of 7 g/cm^3, which is about 30% smaller than that of bulk liquid Pd, and the smaller particles have even smaller

DOI: 10.1021/acs.jpcc.5b01226
J. Phys. Chem. C 2015, 119, 19073−19082

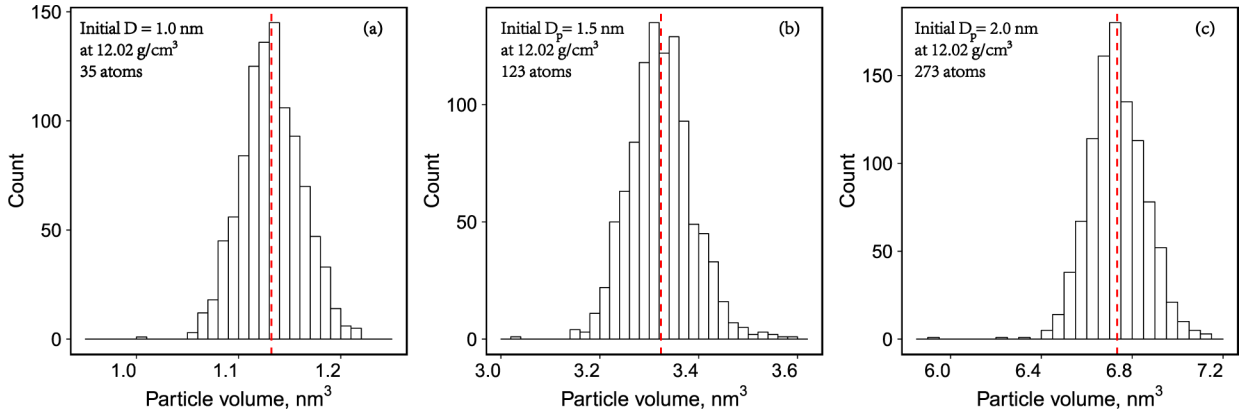

Figure 9. MD predictions of Pd particle size. The vertical dashed lines represent the average volumes of 1000 snapshots taken from a 100 ps trajectory, 1.13 ± 0.03 nm^3 (a), 3.32 ± 0.06 nm^3 (b), and 6.73 ± 0.12 nm^3 (c). The corresponding density is 5.47 ± 0.14 g/cm^3 (a), 6.54 ± 0.12 g/cm^3 (b), and 7.10 ± 0.15 g/cm^3 (c).

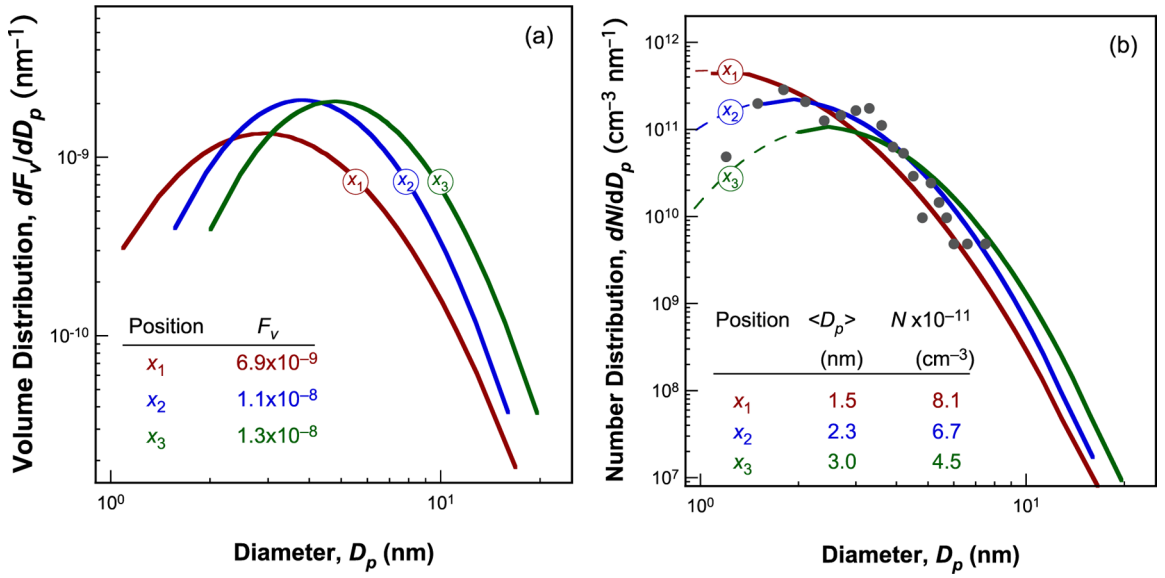

Figure 10. Volume (a) and number (b) distributions from fitting SAXS data (solid lines). Dashed lines show extrapolation of the fitted log-normal distribution functions to smaller sizes. Symbols are the normalized number distribution of the primary particles determined from TEM images, multiplied by 5 × 10^{11} cm^{-3}.

mass density. Here, the MD-based ρ_m value of 7 g/cm^3 was used for SAXS data interpretation (i.e., eq 4).

3.5. SAXS Data Interpretation and Size Distributions. The particle MD information was used to fit the SAXS data to extract the particle size distributions. The data in Figure 2 was fitted using the Modeling II tool in the Irena package[47] within the Igor Pro analysis and plotting program. The fitting is based on eq 8 for polydisperse particles, using the form factor for spheres.

The fitted intensity models are shown as smooth curves in Figure 2. The extracted volume-weighted and number-weighted size distributions are presented in parts a and b, respectively, of Figure 10. As expected, the particle size increases with increasing residence time as the particles nucleate in the flame front and move toward the stagnation surface. Integrating the volume distribution curves of Figure 10a shows that the volume fraction increases, from F_v = 6.9 × 10^{-9}, 1.1 × 10^{-8} to 1.3 × 10^{-8} for x_1, x_2 to x_3, respectively. These values demonstrate the high sensitivity of the SAXS measurement—nanometer-sized particles with volume loading as small as roughly 10^{-8} can be detected and quantified. The number density of the particles decreases, however, from N = 8.1 × 10^{11}, 6.7 × 10^{11} to 4.5 × 10^{11} (cm^{-3}), for x_1, x_2 to x_3, respectively, as one would expect for a particle formation mechanism dominated by gas-phase nucleation followed by particle−particle coalescence, which reduces the number concentration.

Figure 10b compares the number-weighted size distributions extracted from SAXS (solid curves) to the normalized number-weighted distribution of the primary particles obtained from the TEM images (data points). Considering that the SAXS data sample radially across the flame, while the TEM grids were positioned outside the flame near the stagnation plate, the agreement is reasonable and consistent with the small variations of particle size at the three positions SAXS probed, as shown in Figure 10b. The median diameter of the log-normal size distributions of Figure 10b is $<D_p>$ = 1.5, 2.3, and 3.0 nm at x_1, x_2 and x_3, respectively. These values also are in reasonable agreement with the mean particle size of about 2.5 nm from TEM. The geometric standard deviation of the SAXS number

DOI: 10.1021/acs.jpcc.5b01226
J. Phys. Chem. C 2015, 119, 19073−19082

distribution is between 1.6 and 1.8. These values are consistent with the vapor-phase nucleation and growth mechanism that would produce a limiting standard deviation of 1.46 for a self-preserved distribution.[25,26] Again, a fragmentation-based mechanism is expected to produce a substantially wider size distribution that can range from the molecular size to as large as tens of nanometers.

As mentioned above, the air background can be contaminated by particles that escape the flame, even though the majority of the particles should have been sequestered by the cold stagnation surface. We estimate that the error in the absolute volumes and numbers of particles could be 40−50%.

The relative shapes of the size distributions are more accurate, with error estimated to be 10−25%.

3.6. Aerosol Dynamics Simulations. Number-weighted size distributions calculated via the aerosol dynamics simulation discussed above are shown in Figure 11 for two values of the

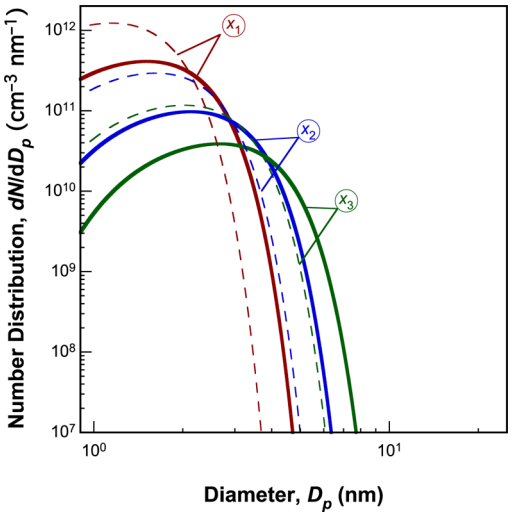

Figure 11. Number distributions computed with the collision enhancement factor ε = 8 (solid lines) and ε = 4 (dashed lines).

collision enhancement factor, ε = 8 and 4. The computed number distributions are all narrower than the SAXS data. The difference suggests that trace particles in the gas outside the flame and/or those deposited on the windows can increase the SAXS background signal, especially for the large particle sizes. The sizes of these "background" particles are expected to be larger than those in the flames because they have had longer times to grow.

The median diameter of the number distribution observed by SAXS is matched by the simulation for ε = 8, assuming unit sticking probability (solid lines of Figure 11). For ε = 4, the computed growth rates are too small when compared to the experiment: the median diameter is underpredicted and the number density is overpredicted (dashed lines of Figure 11). Based on the potential function for interaction of palladium given by Böyükata and Belchior,[48] the reduced Hamaker constant of Pd is estimated to be 80 at 2200 K. For charged particles with Knudsen number Kn = 100, the collision enhancement factor lies between 7 and 16, depending the size ratio of the two colliding particles.[49] If the collision pair is both neutral, the collision process is influenced by the van der Waals interaction only and the enhancement factor should be substantially smaller. The computational results suggest that at least some of the particles are electrically charged during their size growth. It was demonstrated previously[50] that over 50% of carbon nanoparticles in flames are either positively or negatively charged at 2000 K. The work function for Pd is 5.12 eV, which is only slightly larger than that of carbon (4.81 eV). Hence, it is not unexpected a significant fraction of Pd particles would be charged, leading to the relatively large ε value that is required to reproduce the experimental growth rate.

4. CONCLUSIONS

The formation and growth of palladium nanoparticles in a fuel-lean premixed stagnation-flow ethylene flame has been investigated using in situ small-angle X-ray scattering. The particles are formed by decomposition of the molecular precursor $Pd(acetate)_2$, leading to aggregation of the resulting Pd atoms to form particles. SAXS was used to detect and quantify the particle size distribution function at several positions in the flame, and the in situ SAXS results were confirmed by ex situ measurements by TEM. The following conclusions may be drawn from the experimental and computational results:

(1) The particles are just a few nanometers in diameter and are molten Pd in the flame. They crystallized outside the flame as they collected for the TEM measurement.

(2) Particles as small as 1 nm in diameter are detected by SAXS. The particles nucleate in the flame front following the dissociation of $Pd(acetate)_2$. This is followed by size and mass growth following a coalescence mechanism.

(3) The Pd atom-particle and particle−particle sticking probability appears to be close to unity and a large value of the collision enhancement factor is required for the aerosol dynamic simulation to reproduce the evolution of the size distribution as measured by SAXS, suggesting that a substantial fraction of the particles are electrically charged in the flame.

(4) Molecular dynamics results demonstrate that at the temperature of interest the particles undergo substantial thermal expansion. At 2000 K, the mass density of the particle material is 7 g/cm^3 for a 273 atm particle, which is substantially smaller than that of bulk, liquid Pd at its melting point.

(5) We demonstrate that an appropriate SAXS data interpretation for ultrafine particles in a gaseous flame requires careful considerations of the temperature and size effect on the mass density of the particle material in addition to the particle composition and phase.

AUTHOR INFORMATION

Corresponding Author

*E-mail: rewinans@anl.gov.

Notes

The authors declare no competing financial interest.

ACKNOWLEDGMENTS

We thank Dr. Byeongdu Lee and Dr. Xiaobing Zuo for their help with the SAXS data analysis. We also thank Dr. Jan Ilavsky for providing the "IRENA" macro package for Igor Pro for the data fitting. Use of the Advanced Photon Source, an Office of Science User Facility operated for the U.S. Department of Energy (DOE) Office of Science by Argonne National Laboratory, was supported by the U.S. DOE under Contract No. DE-AC02-06CH11357. This work was performed, in part, at the Center for Nanoscale Materials, a U.S. Department of

DOI: 10.1021/acs.jpcc.5b01226
J. Phys. Chem. C 2015, 119, 19073−19082

Energy, Office of Science, Office of Basic Energy Sciences User Facility under Contract No. DE-AC02-06CH11357. The Argonne, Utah, USC, and Stanford groups gratefully acknowledge support for this work from the Molecular Dynamics program of the Air Force Office of Scientific Research (AFOSR) through a MURI grant (FA9550-08-1-0400).

REFERENCES

(1) Kappenstein, C. J.; Batonneau, Y.; Brahmi, R.; Pirault-Roy, L. Propulsion and Catalysis - Historical Survey, up-to-Date Overview, and Current Challenges. *Int. J. Energ. Mater. Chem. Propul.* **2010**, *9*, 413−436.

(2) Wickham, D. T.; Cook, R.; De Voss, S.; Engel, J. R.; Nabity, J. Soluble Nano-Catalysts for High Performance Fuels. *J. Russ. Laser Res.* **2006**, *27*, 552−561.

(3) Shimizu, T.; et al. Methane Ignition Catalyzed by in Situ Generated Palladium Nanoparticles. *Combust. Flame* **2010**, *157*, 421−435.

(4) Van Devener, B.; Anderson, S. L.; Shimizu, T.; Wang, H.; Nabity, J.; Engel, J.; Yu, J.; Wickham, D.; Williams, S. In Situ Generation of Pd/Pdo Nanoparticle Methane Combustion Catalyst: Correlation of Particle Surface Chemistry with Ignition. *J. Phys. Chem. C* **2009**, *113*, 20632−20639.

(5) Sabourin, J. L.; Dabbs, D. M.; Yetter, R. A.; Dryer, F. L.; Aksay, I. A. Functionalized Graphene Sheet Colloids for Enhanced Fuel/Propellant Combustion. *ACS Nano* **2009**, *3*, 3945−3954.

(6) Wang, J. W.; Liu, Y.; Zhang, X. W.; Mi, Z. T.; Wang, L. Facile Preparation of Hydrocarbon Fuel-Soluble Nano-Catalyst and Its Novel Application in Catalytic Combustion of Jp-10. *Catal. Commun.* **2009**, *10*, 1518−1522.

(7) Van Devener, B.; Perez, J. P. L.; Jankovich, J.; Anderson, S. L. Oxide-Free, Catalyst-Coated, Fuel-Soluble, Air-Stable Boron Nanopowder as Combined Combustion Catalyst and High Energy Density Fuel. *Energy Fuels* **2009**, *23*, 6111−6120.

(8) Mirzajanzadeh, M.; Tabatabaei, M.; Ardjmand, M.; Rashidi, A.; Ghobadian, B.; Barkhi, M.; Pazouki, M. A Novel Soluble Nano-Catalysts in Diesel-Biodiesel Fuel Blends to Improve Diesel Engines Performance and Reduce Exhaust Emissions. *Fuel* **2015**, *139*, 374−382.

(9) E, X. T. F.; Zhang, Y.; Zou, J. J.; Wang, L.; Zhang, X. E. Oleylamine-Protected Metal (Pt, Pd) Nanoparticles for Pseudohomogeneous Catalytic Cracking of Jp-10 Jet Fuel. *Ind. Eng. Chem. Res.* **2014**, *53*, 12312−12318.

(10) Wang, J.; Winans, R. E.; Anderson, S. L.; Seifert, S.; Lee, B.; Chupas, P. J.; Ren, Y.; Lee, S.; Liu, Y. Z. In Situ Small-Angle X-Ray Scattering from Pd Nanoparticles Formed by Thermal Decomposition of Organo-Pd Catalyst Precursors Dissolved in Hydrocarbons. *J. Phys. Chem. C* **2013**, *117*, 22627−22635.

(11) England, W. A. An Insitu X-Ray Small-Angle Scattering Study of Soot Morphology in Flames. *Combust. Sci. Technol.* **1986**, *46*, 83−93.

(12) Hessler, J. P.; Seifert, S.; Winans, R. E. Spatially Resolved Small-Angle X-Ray Scattering Studies of Soot Inception and Growth. *Proc. Combust. Inst.* **2002**, *29*, 2743−2748.

(13) Gardner, C.; Greaves, G. N.; Hargrave, G. K.; Jarvis, S.; Wildman, P.; Meneau, F.; Bras, W.; Thomas, G. In Situ Measurements of Soot Formation in Simple Flames Using Small Angle X-Ray Scattering. *Nucl. Instrum. Methods Phys. Res., Sect. B* **2005**, *238*, 334−339.

(14) di Stasio, S.; Mitchell, J. B. A.; LeGarrec, J. L.; Biennier, L.; Wulff, M. Synchrotron Saxs (in Situ) Identification of Three Different Size Modes for Soot Nanoparticles in a Diffusion Flame. *Carbon* **2006**, *44*, 1267−1279.

(15) Mitchell, J. B. A.; Courbe, J.; Florescu-Mitchell, A. I.; di Stasio, S.; Weiss, T. Demonstration of Soot Particle Resizing in an Ethylene Flame by Small Angle X-Ray Scattering. *J. Appl. Phys.* **2006**, *100*, 124918.

(16) Mitchell, J. B. A.; di Stasio, S.; LeGarrec, J. L.; Florescu-Mitchell, A. I.; Narayanan, T.; Sztucki, M. Small Angle X-Ray Scattering Study of Flame Soot Nanoparticle Aggregation and Restructuring. *J. Appl. Phys.* **2009**, *105*, 124904.

(17) Ossler, F.; Canton, S. E.; Larsson, J. X-Ray Scattering Studies of the Generation of Carbon Nanoparticles in Flames and Their Transition from Gas Phase to Condensed Phase. *Carbon* **2009**, *47*, 3498−3507.

(18) Ossler, F.; Vallenhag, L.; Canton, S. E.; Mitchell, J. B. A.; Le Garrec, J.-L.; Sztucki, M.; di Stasio, S. Dynamics of Incipient Carbon Particle Formation in a Stabilized Ethylene Flame by in Situ Extended-Small-Angle- and Wide-Angle X-Ray Scattering. *Carbon* **2013**, *51*, 1−19.

(19) Sztucki, M.; Narayanan, T.; Beaucage, G. In Situ Study of Aggregation of Soot Particles in an Acetylene Flame by Small-Angle X-Ray Scattering. *J. Appl. Phys.* **2007**, *101*, 114304.

(20) Beaucage, G.; Kammler, H. K.; Mueller, R.; Strobel, R.; Agashe, N.; Pratsinis, S. E.; Narayanan, T. Probing the Dynamics of Nanoparticle Growth in a Flame Using Synchrotron Radiation. *Nat. Mater.* **2004**, *3*, 370−374.

(21) Kammler, H. K.; Beaucage, G.; Kohls, D. J.; Agashe, N.; Ilavsky, J., Monitoring Simultaneously the Growth of Nanoparticles and Aggregates by in Situ Ultra-Small-Angle X-Ray Scattering. *J. Appl. Phys.* **2005**, *97*.05430910.1063/1.1855391

(22) Feigin, L. A.; Svergun, D. I. *Structure Analysis by Small-Angle X-Ray and Neutron Scattering*; Plenum: New York, 1987; p xiii + 335.

(23) Narayanan, T., In *Lecture Notes in Physics (Non-Crystalline Diffraction)*; Ezquerra, T., Ed.; Springer: Berlin, Heidelberg, 2009; Vol. *776*, p 133.

(24) Pedersen, J. S. Analysis of Small-Angle Scattering Data from Colloids and Polymer Solutions: Modeling and Least-Squares Fitting. *Adv. Colloid Interface Sci.* **1997**, *70*, 171.

(25) Lai, F. S.; Hidy, G. M.; Friedlander, S. K.; Pich, J. Self-Preserving Particle-Size Distribution for Brownian Coagulation in Free-Molecule Regime. *J. Colloid Interface Sci.* **1972**, *39*, 395.

(26) Landgrebe, J. D.; Pratsinis, S. E. A Discrete-Sectional Model for Particulate Production by Gas-Phase Chemical-Reaction and Aerosol Coagulation in the Free-Molecular Regime. *J. Colloid Interface Sci.* **1990**, *139*, 63−86.

(27) Zhao, B.; Uchikawa, K.; McCormick, J. R.; Ni, C. Y.; Chen, J. G.; Wang, H. Ultrafine Anatase TiO_2 Nanoparticles Produced in Premixed Ethylene Stagnation Flame at 1 Atm. *Proc. Combust. Inst.* **2004**, *30*, 2569−2576.

(28) Tolmachoff, E. D.; Abid, A. D.; Phares, D. J.; Campbell, C. S.; Wang, H. Synthesis of Nano-Phase TiO_2 Crystalline Films over Premixed Stagnation Flames. *Proc. Combust. Inst.* **2009**, *32*, 1839−1845.

(29) Lutz, A. E.; Kee, R. J.; Grcar, J. F.; Rupley, F. M. *Oppdif: A Fortran Program for Computing Opposed-Flow Diffusion Flames*; Sandia National Laoratories Report SAND96-8243; Sandia National Laboratories: Albuquerque, 1997.

(30) Wang, H.; You, X.; Joshi, A. V.; Davis, S. G.; Laskin, A.; Egolfopoulos, F.; Law, C. K., High-Temperature Combustion Reaction Model of $H_2/CO/C_1$-C_4 Compounds. In *High-Temperature Combustion Reaction Model of $H_2/CO/C_1$-C_4 Compounds*; US Combustion Laboratory: Los Angeles, 2007; http://ignis.usc.edu/USC_Mech_II.htm.

(31) Zhao, B.; Yang, Z.; Johnston, M. V.; Wang, H.; Wexler, A. S.; Balthasar, M.; Kraft, M. Measurement and Numerical Simulation of Soot Particle Size Distribution Functions in a Laminar Premixed Ethylene-Oxygen-Argon Flame. *Combust. Flame* **2003**, *133*, 173−188.

(32) Cleri, F.; Rosato, V. Tight-Binding Potentials for Transition-Metals and Alloys. *Phys. Rev. B: Condens. Matter Mater. Phys.* **1993**, *48*, 22−33.

(33) Li, Z.; Wang, H. Gas-Nanoparticle Scattering: A Molecular View of Momentum Accommodation Function. *Phys. Rev. Lett.* **2005**, *95*, 014502.

(34) Beeman, D. Some Multistep Methods for Use in Molecular-Dynamics Calculations. *J. Comput. Phys.* **1976**, *20*, 130−139.

DOI: 10.1021/acs.jpcc.5b01226
J. Phys. Chem. C 2015, 119, 19073−19082

(35) Totton, T. S.; Chakrabarti, D.; Misquitta, A. J.; Sander, M.; Wales, D. J.; Kraft, M. Modelling the Internal Structure of Nascent Soot Particles. *Combust. Flame* **2010**, *157*, 909−914.
(36) Bondi, A. Van Der Waals Volumes + Radii. *J. Phys. Chem.* **1964**, *68*, 441.
(37) Chen, D.; Akroyd, J.; Mosbach, S.; Kraft, M. Surface Reactivity of Polycyclic Aromatic Hydrocarbon Clusters. *Proc. Combust. Inst.* **2015**, *35*, 1811−1818.
(38) Gallagher, P. K.; Gross, M. E. The Thermal Decomposition of Palladium Acetate. *J. Therm. Anal.* **1986**, *31*, 1231−1241.
(39) Hull, A. W.; Davey, W. P. Graphical Determination of Hexagonal and Tetragonal Crystal Structures from X-Ray Data. *Phys. Rev.* **1921**, *17*, 549−570.
(40) Law, C. K. *Combustion Physics*; Cambridge University Press: Cambridge, 2006.
(41) Lide, D. R. *CRC Handbook of Chemistry and Physics*, 86th ed.; CRC Press: Boca Raton, 2005.
(42) Buffat, P.; Borel, J. P. Size Effect on the Melting Temperature of Gold Particles. *Phys. Rev. A: At., Mol., Opt. Phys.* **1976**, *13*, 2287.
(43) Hildenbrand, D. L.; Lau, K. H. Dissociation Energy of the Pdo Molecule. *Chem. Phys. Lett.* **2000**, *319*, 95−98.
(44) Campbell, M. L.; Plane, J. M. C. Kinetic Study of the Recombination Reaction of Gas Phase Pd(a(1)S(0)) with O_2 from 294 to 523 K. *J. Phys. Chem. A* **2003**, *107*, 3747−3751.
(45) Rao, Y. K. *Stoichiometry and Thermodynamics of Metallurgical Processes*; CUP Archive: Cambridge, 1985.
(46) Li, Z.; Wang, H. Thermophoretic Force and Velocity of Nanoparticles in the Free Molecule Regime. *Phys. Rev. E* **2004**, *70*, 021205.
(47) Ilavsky, J.; Jemian, P. R. Irena: Tool Suite for Modeling and Analysis of Small-Angle Scattering. *J. Appl. Crystallogr.* **2009**, *42*, 347−353.
(48) Böyükata, M.; Belchior, J. C. Molecular Dynamics Study of Palladium Clusters: Size Dependent Analysis of Structural Stabilities and Energetics of Pd(N) ($N \leq 40$) Via a Lennard-Jones Type Potential. *Croat. Chem. Acta* **2008**, *81*, 289−297.
(49) Huang, D. D.; Seinfeld, J. H.; Okuyama, K. Image Potential between a Charged Particle and an Uncharged Particle in Aerosol Coagulation–Enhancement in All Size Regimes and Interplay with Van Der Waals Forces. *J. Colloid Interface Sci.* **1991**, *141*, 191−198.
(50) Balthasar, M.; Mauss, F.; Wang, H. A Computational Study of the Thermal Ionization of Soot Particles and Its Effect on Their Growth in Laminar Premixed Flames. *Combust. Flame* **2002**, *129*, 204−216.

DOI: 10.1021/acs.jpcc.5b01226
J. Phys. Chem. C 2015, 119, 19073−19082